RSC Advances

PAPER

Cite this: *RSC Adv.*, 2015, **5**, 49765

High performance NiO microsphere anode assembled from porous nanosheets for lithium-ion batteries

Lihua Chu,[a] Meicheng Li,*[ab] Xiaodan Li,[a] Yu Wang,[a] Zipei Wan,[a] Shangyi Dou,[a] Dandan Song,[a] Yingfeng Li[a] and Bing Jiang[a]

Received 31st March 2015
Accepted 12th May 2015

DOI: 10.1039/c5ra05659d

www.rsc.org/advances

3D NiO microspheres assembled from porous nanosheets are prepared and evaluated as an anode material for lithium-ion batteries, showing excellent electrochemical performance with high lithium storage capacity, and satisfactory cyclability and rate performance. The NiO microspheres deliver a first discharge capacity of 1242 mA h g^{-1} with a reversible capacity up to 820 mA h g^{-1} after 100 cycles at a current of 100 mA g^{-1} in a half cell, also exhibiting an ameliorative rate capacity of 634 mA h g^{-1} at the current of 1 A g^{-1}. The high lithium storage performance can be mainly ascribed to the porous nanosheets, which improve lithium ion transfer, provide sufficient electrode/electrolyte contact areas, and more efficiently accommodate the volume change that occurs with the lithiation/delithiation process. Moreover, the 3D microsphere architecture is also helpful for enhancing the electrochemical performance of the lithium-ion battery. The results indicate the great potential of the 3D NiO microspheres assembled from porous nanosheets for use as an anode material for lithium-ion batteries.

Introduction

With the rapid development of the global economy, the fast depletion of non-renewable energy, and the increasing environmental problems, it is urgent to develop new clean and sustainable sources of energy and new technologies for energy storage and energy conversion with high efficiency.[1–3] Rechargeable lithium-ion batteries (LIBs) are one promising energy storage and conversion technology for the upcoming high demand such as electric vehicles and grid storage systems because of their high energy density, long lifespan, lack of a memory effect, and environmental benignancy.[4] Currently, commercially used graphite anode materials with low specific capacity (theoretical capacity is 372 mA h g^{-1}) and low lithium ion mobility are not sufficient to meet the demands of modern development. Hence, alternative anode materials with higher capacities are urgently needed to increase the energy density and performance of lithium-ion batteries.

A series of transition metal oxides has been exploited for use as anode materials in LIBs.[5–7] Among these, NiO has drawn attention because of its high theoretical capacity (717 mA h g^{-1}), high abundance, non-toxicity, environmental benignity, and low cost. However, the practical utilization of NiO is still low because of its poor rate performances and insufficient cycling due to the poor conductivity, volume change, and subsequent particle pulverization upon lithiation/delithiation.[8] Therefore, it is crucial to increase the lithium ion mobility, mitigate the pulverization, and further enhance the structural stability. To date, several strategies have been undertaken to enhance the performance of NiO electrode materials. One well-established method relies on the design and synthesis of nanostructured materials such as microspheres,[9] nanosheets,[10] three-dimensional (3D) flower-like hierarchical architectures,[11] and nanotubes,[12] expecting to promote the electrochemical performance and maintain good structural integration. The most popular among various kinds of nanostructured electrode materials are porous ones, which provide the structural flexibility for volume change and the routes for fast Li^+ diffusion leading to enhanced performance.[9,13,14] Therefore, in consideration of the strategy mentioned above, constructing porous nanoarchitecture is meaningful to enhance the electrochemical performance of LIBs.

Herein, we describe our design for a 3D NiO microsphere architecture assembled from porous nanosheets that can be used as an anode material in lithium-ion batteries. The advantages of the combination of the porous nanosheets and 3D architecture endow the as-prepared 3D NiO microspheres with a good performance of stable and high reversible discharge capacity up to 820 mA h g^{-1} even after 100 cycles at a current density of 100 mA g^{-1}, and a good rate capability of 634 mA h g^{-1} at a high current density of 1 A g^{-1}, which opens up new opportunities in the development of high performance LIBs.

[a]*State Key Laboratory of Alternate Electrical Power Systems with Renewable Energy Sources, North China Electric Power University, Beijing, 102206, China. E-mail: mcli@ncepu.edu.cn; Fax: +86 10 6177 2951; Tel: +86 10 6177 2951*

[b]*Chongqing Materials Research Institute, Chongqing 400707, China*

Experimental

Synthesis of 3D NiO microspheres

The 3D NiO microspheres were prepared by precipitation and a hydrothermal process. All reagents used in the experiments were of analytical grade and used without further purification. Distilled water was used for all syntheses and treatment processes. $Ni(OH)_2$ was prepared by dissolving 0.7134 g of $Ni(NO_3)_2 \cdot 6H_2O$ and 0.25 g of polyvinyl pyrrolidone K30 (PVP-K30) in 40 mL of distilled water, adjusting the pH to 10.9 with ammonia and a pH meter, and using a magnetic stirrer to form a homogeneous solution at room temperature. The solution was then transferred into a Teflon-lined stainless steel autoclave (50 mL), sealed, and heated to 150 °C for 15 h. The greenish product was collected by centrifugation, washed with deionized water and ethanol several times to remove impurities, and then dried at 60 °C in vacuum. Finally, the NiO nanostructures were obtained by heating the hydroxide precursor at 600 °C for 2 h in air.

Material characterization

The morphology of the as-synthesized NiO products was observed by FEI Quanta 200F field emission scanning electron microscopy (FESEM) and Tecnai G2 F20 field emission transmission electron microscopy (TEM) with accelerating voltage of 200 kV. The crystalline phase was identified with a Bruker D8 Focus X-ray powder diffractometer using Cu K_α ($\lambda = 1.5406$ Å) radiation over a range of 2θ from 20° to 90°. The thermogravimetric/differential thermal analysis (TG/DTA) measurement was performed using a STA6000 thermogravimetric analyzer in air at a scan rate of 10 °C min^{-1} from room temperature to 600 °C. Brunauer–Emmett–Teller (BET) surface areas of the samples were analyzed by nitrogen adsorption–desorption measurements on a Quantachrome Autosorb-IQ-MP sorption analyzer with prior degassing under vacuum at 77 K. The pore size distribution was derived from a desorption branch by a Barrett–Joyner–Halenda (BJH) method.

Electrochemical measurement

The working electrodes were fabricated by coating a copper foil with a slurry containing 80 wt% of 3D NiO microspheres, 10 wt% of acetylene black (Super-P), and 10 wt% of polyimide dissolved in *N*-methyl-2-pyrrolidinone and drying at 300 °C in vacuum for 2 h before pressing. Standard CR2032-type coin cells were assembled in an Ar-filled glove box (KIYON, Korea) using the as-prepared anode, Li metal foil (0.4 mm thick) as the counter electrode, and a separator (Solupor 7P03A). The electrolyte was 1 M $LiPF_6$ dissolved in a mixture of ethylene carbonate (EC) and dimethyl carbonate (DMC) (v/v = 1 : 1). The cells were aged for 12 h before the measurements. Galvanostatic discharge–charge (GDC) experiments were performed at different current densities in the voltage range of 0.01–3.00 V with a multichannel battery tester (Maccor, Inc, USA). Cyclic voltammetry (CV) measurements were conducted with an electrochemical workstation (Solartron Potentiostat and Impedance Analyser, UK). Electrochemical impedance spectra (EIS) were measured using the same electrochemical workstation by applying an AC voltage of 10 mV amplitude over a frequency range from 100 kHz to 100 mHz.

Results and discussion

The prepared NiO product shows excellent crystallinity, as evidenced by powder X-ray diffraction (XRD) results. The XRD spectra are shown in Fig. 1. All of the observed diffraction peaks can be perfectly indexed to the pure NiO products with a face-centred cubic phase (JCPDS no. 47-1049, space group *Fm*3*m*). The diffraction peaks at 37.24°, 43.27°, 62.87°, 75.41°, and 79.41° correspond to the (111), (200), (220), (311), and (222) planes, respectively. The sharp diffraction peaks reflect the excellent crystallinity of NiO. Moreover, no other peaks arising from impurities can be observed, indicating the pure phase of the as-prepared NiO product.

The morphology and architecture of the as-prepared NiO product were visualized by scanning electron microscopy (SEM) and transmission electron microscopy (TEM). The corresponding images are shown in Fig. 2. From the low-magnification FESEM image (Fig. 2(a)), it can be observed that the product shows a uniform 3D microsphere architecture. The high-magnification image (Fig. 2(b)) clearly shows that the microspheres have a size of 2–3 μm and are composed of assembled porous nanosheets. The TEM image (Fig. 2(d)) further depicts that the nanosheets are porous,[15] with a pore diameter of approximately 5 nm, which could facilitate lithium ion migration and buffer the volume change during the lithiation/delithiation process.[10,16] The formation of the pores should be credited to the decomposition of $Ni(OH)_2$ precursors and the high reaction/etching rate at the defect sites in the precursor nanosheets during calcination. The high resolution TEM (HRTEM) image of the 3D NiO microspheres and their corresponding fast Fourier transform (FFT) pattern are shown in Fig. 2(e) and (f). The interplanar spacing of 2.4 Å and 1.5 Å of the resolved lattice fringes are consistent with the (111) and (220) planes of the NiO crystal, respectively.

The thermal decomposition behavior of the as-synthesized $Ni(OH)_2$ precursor was evaluated by TG/DTA measurement to

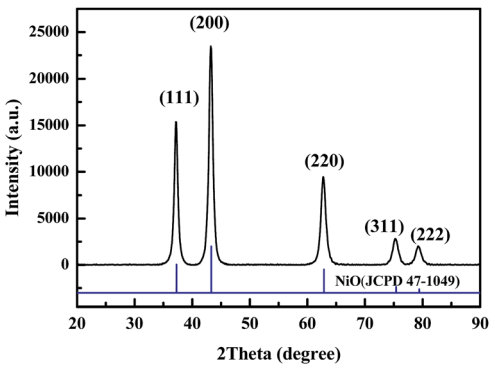

Fig. 1 The X-ray diffraction pattern of 3D porous nanosheet-assembled NiO microspheres obtained at room temperature as well as the standard JCPD card of NiO.

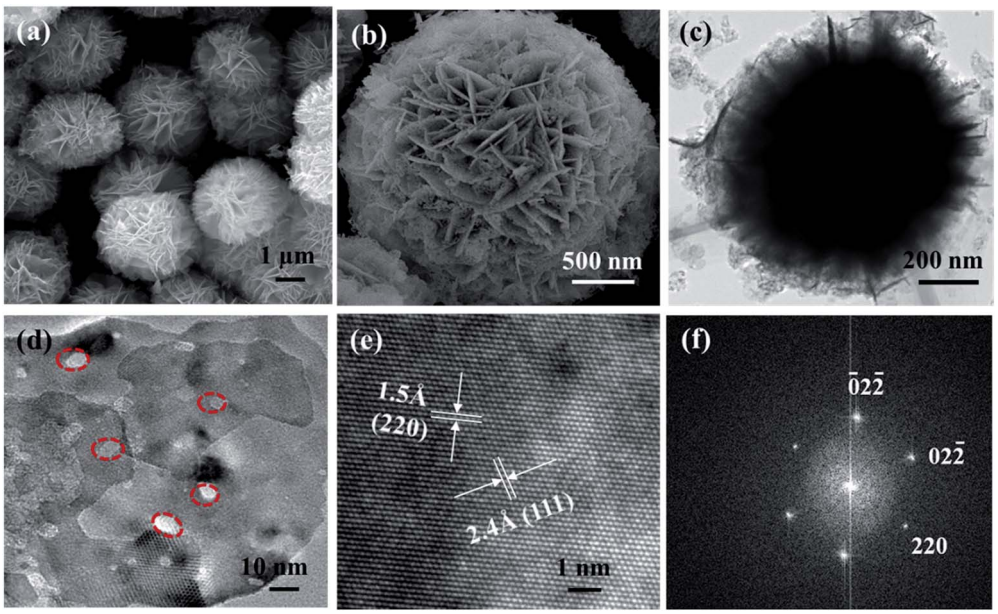

Fig. 2 (a) Low- and (b) high-magnification SEM images of the porous nanosheet-assembled NiO microspheres, (c) and (d) TEM images, (e) HRTEM image of the porous nanosheet-assembled NiO microspheres, and (f) HRTEM image of their corresponding fast Fourier transform (FFT) pattern.

study the conversion process. Fig. 3 shows the endothermic peak at 314 °C in the derivative weight curve. The weight loss of 22% is attributed to the solvent evaporation and thermal decomposition of $Ni(OH)_2$ to NiO. The observed weight loss is close to the calculated loss value of 19.4%. No weight loss could be observed above 550 °C. Thus, it is concluded that the $Ni(OH)_2$ precursor can decompose to form NiO above 314 °C. In our experiment, a calcining temperature of 600 °C was used, and thus, a pure NiO phase was obtained.

To further present specific textural properties of the as-prepared NiO microspheres, the specific surface area was characterized by BET nitrogen adsorption–desorption analysis, as shown in Fig. 4. In terms of shape, the adsorption isotherm can be classified as a type IV curve with type III hysteresis loops, which indicates the existence of slit-shaped pores, according to the IUPAC classification. A distinct hysteresis loop can be observed in the large range of approximately 0–0.98 P/P_0, indicating the existence of mesopores and macropores.[17] The BJH pore size distribution calculated from the adsorption branch is presented as the inset in Fig. 4. The first peak at the mean value of 4.3 nm is due to mesoporous channels, which is consistent with the TEM observations, indicating that the NiO pores are uniform with a narrow pore size distribution. In addition, the mesoporous volume is 0.64 $cm^3\ g^{-1}$. The pores at approximately 61 nm are related to the interspace between the NiO nanosheets. Moreover, the surface area is approximately 83.97 $m^2\ g^{-1}$, which is similar to the value obtained for mesoporous NiO.[8,18]

The lithium storage properties of the as-prepared 3D NiO microsphere-assembled porous nanosheets were investigated by CV and discharge–charge measurements in a half-cell configuration. The CV curves for the first 5 cycles at the

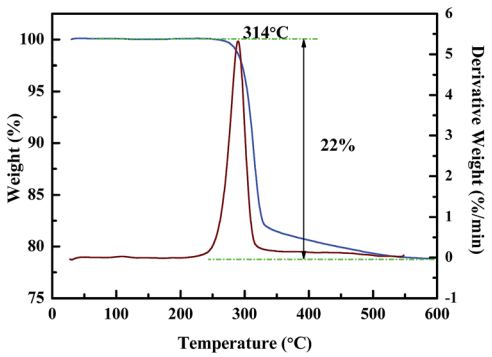

Fig. 3 TG/DTA curves of the porous nanosheet-assembled NiO microspheres.

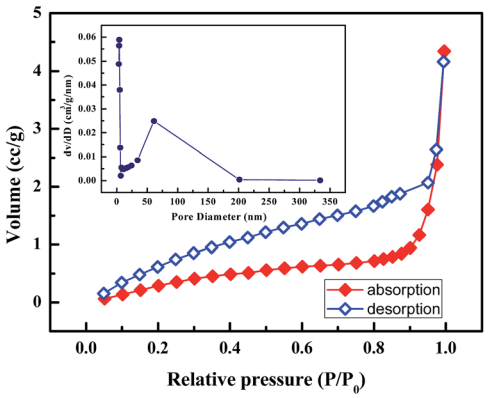

Fig. 4 Nitrogen adsorption–desorption isotherms of the porous nanosheet-assembled NiO obtained by hydrothermal synthesis.

scanning rate of 0.5 mV s^{-1} are shown in Fig. 5(a). In the first scanning cycle, one characteristic cathodic peak appeared at approximately 0.3 V, indicating the reduction of Ni^{2+} to Ni and association with the lithiation reaction to form Li_2O and a partially irreversible solid electrolyte interphase (SEI) film formation. In the subsequent cycles, the cathodic peak potentials shift to 1.0 V and become smaller, indicating that an irreversible reaction is present in the first cycle. Two anodic peaks are present at approximately 1.6 and 2.2 V during the charge cycle, corresponding to the decomposition of electrolyte and Li_2O accompanying the oxidation of Ni.[8,10,16,19] The redox reaction of lithium ions with the NiO microsphere electrode can be summarized as follows:

$$NiO + 2Li^+ + 2e^- \leftrightarrow Ni + Li_2O \quad (1)$$

$$2Li \leftrightarrow 2Li^+ + 2e^- \quad (2)$$

$$NiO + 2Li \leftrightarrow Ni + Li_2O \quad (3)$$

Fig. 5(b) presents the galvanostatic discharge–charge (GDC) voltage profiles of the porous nanosheet-assembled NiO microspheres obtained at a current density of 100 mA g^{-1} for 100 cycles. A long voltage plateau is observed at approximately 0.65 V, which is due to the reduction of Ni^{2+} to Ni and the formation of SEI film. The subsequent GDC cycles demonstrate slow sloped profiles, with plateaus at approximately 2.2 V upon charge that primarily correspond to the reversible electrochemical processes of Li_2O. These GDC results are well correlated with the CV results. The initial discharge- and charge-specific capacities are 1242 mA h g^{-1} and 850 mA h g^{-1}, respectively, leading to a relatively high coulombic efficiency (CE) of 68%. The initial capacity loss could be reasonably attributed to the SEI film formation and additional storage of Li^+ in the nanosheet pores or the defects. Moreover, the porous NiO nanosheets are ultrathin, which results in more crystal facets that are exposed to provide additional sites (*e.g.*, more surface defects) for Li^+ storage.[16,19,20]

The NiO microspheres assembled from porous nanosheets also show excellent cycling stability, as presented in Fig. 5(c). The specific discharge capacity of the NiO microspheres still remains at 820 mA h g^{-1} at the rate of 100 mA g^{-1} after 100 cycles. This result is much better than that obtained for 3D flower-like NiO hierarchical architectures (713 mA h g^{-1} at 100 mA g^{-1} after 40 cycles),[11] and hollow NiO nanotubes (726 mA h g^{-1} at 0.2 C after 150 cycles).[21] The columbic efficiencies remain stable in the scale of 98–99%, which increase to almost unity at successive cycles, indicating that the formed SEI film during the first cycle is favorable and stable.[10] Furthermore, the capacity of the NiO microspheres gradually increased during the first ten cycles. This is an active process until the electrolyte completely infiltrates into the anode materials, which is usually observed in porous materials. The NiO porous nanosheets can act as a buffer layer to protect the electrode from pulverization due to the volume change and prevent the aggregation of the active materials upon cycling, which is conducive to achieve long-term, high-capacity performance. Furthermore, the 3D microspheres should also be helpful for keeping the structure stable.

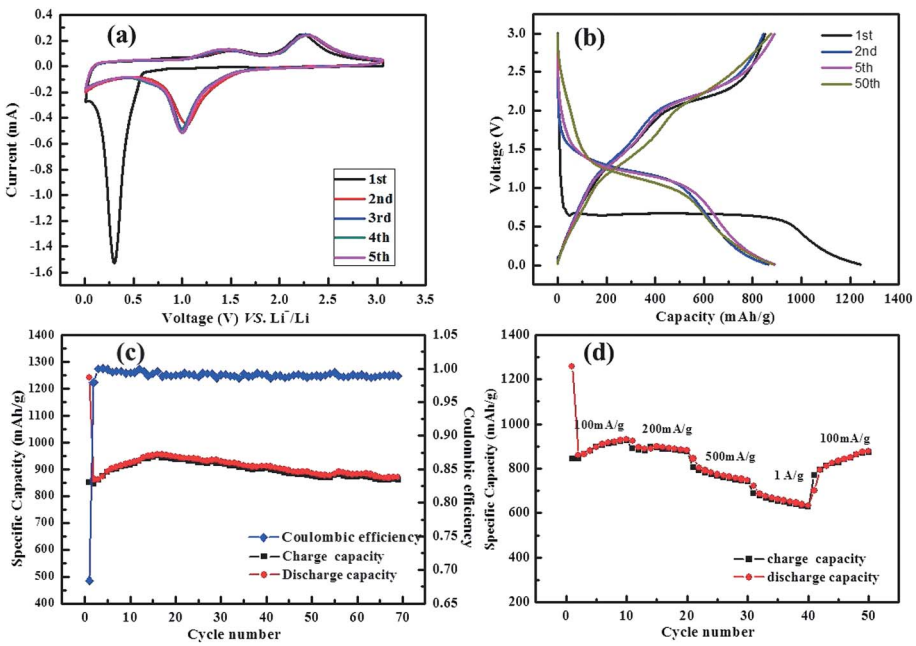

Fig. 5 (a) Representative CVs for the 1st, 2nd, 3rd, 4th, and 5th cycle of the porous nanosheet-assembled NiO microspheres at a scan rate of 0.5 mV s^{-1}, (b) galvanostatic charge–discharge voltage profiles of the NiO microspheres at a current density of 100 mA g^{-1}, (c) comparative cycling performance of the NiO microspheres at a current density of 100 mA g^{-1}, and (d) rate performance of the NiO microspheres at different current densities.

Fig. 5(d) demonstrates the rate capability of NiO microsphere electrodes from current densities of 100 to 1000 mA g^{-1} for ten cycles at each current density. The discharge capacities of NiO microspheres at 100 mA g^{-1}, 200 mA g^{-1}, 500 mA g^{-1}, and 1 A g^{-1} are 932 mA h g^{-1} (10^{th} cycle), 882 mA h g^{-1} (20^{th} cycle), 746 mA h g^{-1} (30^{th} cycle), and 634 mA h g^{-1} (40^{th} cycle), respectively, demonstrating an excellent rate performance for high-power lithium-ion batteries. When the testing current is regularly returned back to the low current rate of 100 mA g^{-1}, the discharge capacities are recovered to the same level compared to the previous cycles that were running at the same currents. The improved rate performance of the NiO microspheres could also be attributed to the ultrathin porous NiO nanosheets. The porous nanosheets can provide sufficient electrode/electrolyte contact areas so that more reaction sites for lithium ion intercalation/de-intercalation would be available. Moreover, the pores are uniform in size and shape, which is favorable for shortening the Li^+ conducting pathways for rapid charge transfer during the lithiation/delithiation process.[8,10,16]

It is worth noting that the NiO microspheres assembled from porous nanosheets show much higher lithium storage capacity, cycle stability, and rate performance than other reported NiO nanostructures,[9,11,21] demonstrating the advantage and high potential of porous nanosheet-assembled NiO microspheres for use as anodes for LIBs.

In order to understand the superior electrochemical performance of the NiO microspheres assembled from porous nanosheets, EIS measurements were carried out before battery cycling tests and after 100 cycles. The Nyquist plots are shown in Fig. 6. Both profiles exhibit a straight line in the low frequency region, which represents typical Warburg behavior related to the diffusion of lithium ions in the active anode materials.[11,22] A single depressed semicircle in the high frequency region observed in the impedance spectra of NiO microspheres before cycling is attributed to the impedance of the charge transfer reaction at the interface of electrolyte and active material. However, the Nyquist plots of NiO microspheres after 100 cycles at the delithiation state are composed of two depressed semicircles, one in the high frequency and one in the middle frequency. The cause of the middle frequency semicircle is the same as that of the one observed in the impedance spectra before cycling. The semicircle observed at the high frequency is due to the formation of the SEI film.[22,23] Moreover, the charge transfer resistance after 100 cycles is lower than that before cycling, further indicating the existence of active processes.

The electrochemical improvement that resulted from use of the as-prepared NiO microspheres assembled from porous nanosheets as the anode for lithium-ion batteries can be reasonably attributed to desirable advantages related to the unique porous architecture with 3D features. As identified by SEM and BET analysis, the NiO microspheres are composed of nanosheets that contain a large amount of pores. The porous nanosheets have the ability to buffer the volume change and prevent the aggregation of the active materials upon cycling, which brings about excellent cycling stability. Moreover, the porous nanosheets can provide sufficient electrode/electrolyte contact areas and facilitate the continuous and rapid electron transport through the electrodes. In addition, the 3D microsphere architecture is helpful for keeping the electrode structure stable upon cycling. Thus, the architecture is able to quickly form a stable SEI film and prevent further decomposition of the electrolyte, resulting in the rapid stabilization of columbic efficiencies of 98–99% and improved rate performance. Furthermore, the porous NiO nanosheets and the SEI film formation contribute most to the long-term high capacity of the as-prepared NiO microspheres for lithium ion storage.[10,19,24,25] Therefore, the unique 3D architecture resulting from the assembled porous nanosheets leads to an anode material for lithium-ion batteries with high capacity and satisfactory cycle stability and rate performance. Thus, the 3D NiO microsphere assembled from porous nanosheets is a promising anode material for high-performance LIBs.

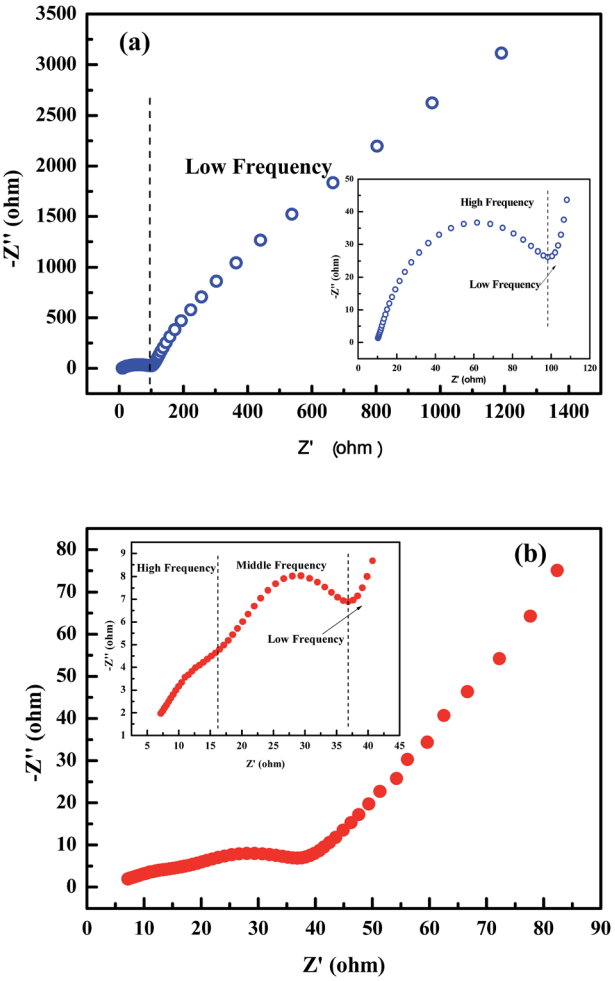

Fig. 6 Electrochemical impedance spectra (100 kHz to 100 mHz) of NiO microspheres: (a) before cycling and (b) after 100 cycles at the delithiation state. The two insets show the corresponding magnified high frequency region of (a) and (b).

Conclusions

In summary, NiO microspheres assembled from porous nanosheets were fabricated and exhibited excellent electrochemical

performance with a reversible discharge capacity up to 820 mA h g^{-1} after 100 cycles at a current of 100 mA g^{-1} and ameliorative rate capacity of 634 mA h g^{-1} at the current of 1 A g^{-1}. These improved and desirable electrochemical performances of the 3D microspheres are primarily attributed to their unique 3D architecture consisting of porous nanosheets. The obtained good performance can be further enhanced so that high-performance LIBs can be used for alternative energy and electric transportation.

Acknowledgements

This work is partially supported by the National High-Tech R&D Program of China (863 Program, no. 2015AA034601), National Natural Science Foundation of China (Grant nos 91333122, 51402106, 51372082, and 51202067), Ph.D. Programs Foundation of Ministry of Education of China (Grant nos 20110036110006, 20120036120006, 20130036110012), Par-Eu Scholars Program, and the Fundamental Research Funds for the Central Universities.

References

1 L. Hu, Z. Tang and Z. Zhang, *J. Power Sources*, 2007, **166**, 226.
2 L. Hu, R. Ma, T. C. Ozawa and T. Sasaki, *Angew. Chem.*, 2009, **121**, 3904.
3 L. Hu, R. Ma, T. C. Ozawa and T. Sasaki, *Inorg. Chem.*, 2010, **49**, 2960.
4 L. Zhang, H. B. Wu and X. W. D. Lou, *Adv. Energy Mater.*, 2014, **4**, 1300958.
5 B. Rangasamy, J. Y. Hwang and W. Choi, *Carbon*, 2014, **77**, 1065–1072.
6 Y. Chen, B. Song, M. Li, L. Lu and J. Xue, *Adv. Funct. Mater.*, 2014, **24**, 319–326.
7 D. S. Guan, J. Y. Li, X. F. Gao and C. Yuan, *RSC Adv.*, 2014, **4**, 4055–4062.
8 H. Liu, G. X. Wang, J. Liu, S. Z. Qiao and H. Ahn, *J. Mater. Chem. Phys.*, 2011, **21**, 3046–3052.
9 D. Xie, W. W. Yuan, Z. M. Dong, Q. M. Su, J. Zhang and G. H. Du, *Electrochim. Acta*, 2013, **92**, 87–92.
10 Y. Huang, X. L. Huang, J. S. Lian, D. Xu, L. M. Wang and X. B. Zhang, *J. Mater. Chem.*, 2012, **22**, 2844.
11 Q. Li, Y. J. Chen, T. Yang, D. N. Lei, G. H. Zhang, L. Mei, L. B. Chen, Q. H. Li and T. H. Wang, *Electrochim. Acta*, 2013, **90**, 80–89.
12 F. Cao, G. X. Pan, X. H. Xia, P. S. Tang and H. F. Chen, *J. Power Sources*, 2014, **264**, 161–167.
13 W. Li, F. Wang, Y. P. Liu, J. X. Wang, J. P. Yang, L. J. Zhang, A. A. Elzatahry, D. Al-Dahyan, Y. Y. Xia and D. Y. Zhao, *Nano Lett.*, 2015, **15**, 2186–2193.
14 L. Y. Shen, Z. X. Wang and L. Q. Chen, *RSC Adv.*, 2014, **4**, 15314.
15 Y. F. Cui, C. Wang, S. J. Wu, G. Liu, F. F. Zhang and T. M. Wang, *CrystEngComm*, 2011, **13**, 4930.
16 D. Xie, Q. M. Su, W. W. Yuan, Z. M. Dong, J. Zhang and G. H. Du, *J. Phys. Chem. C*, 2013, **117**, 24121–24128.
17 H. Wang, L. Y. Shi, T. T. Yan, J. P. Zhang, Q. D. Zhong and D. S. Zhang, *J. Mater. Chem. A*, 2014, **2**, 4739.
18 F. Jiao, A. H. Hill, A. Harrison, A. Berko, A. V. Chadwick and P. G. Bruce, *J. Am. Chem. Soc.*, 2008, **130**, 5262–5266.
19 L. Q. Tao, J. T. Zai, K. X. Wang, Y. H. Wan, H. J. Zhang, C. Yu, Y. L. Xiao and X. F. Qian, *RSC Adv.*, 2012, **2**, 3410.
20 J. S. Gnanaraj, E. Zinigrad, L. Asraf, M. Sprecher, H. E. Gottlieb, W. Geissler, M. Schmidt and D. Aurbach, *Electrochem. Commun.*, 2003, **5**, 946–951.
21 X. Y. Yan, X. L. Tong, J. Wang, C. W. Gong, M. G. Zhang and L. P. Liang, *Mater. Lett.*, 2014, **136**, 74–77.
22 G. M. Zhou, D. W. Wang, L. C. Yin, N. Li, F. Li and H. M. Cheng, *ACS Nano*, 2012, **6**, 3214–3223.
23 J. C. Guo, A. Sun, X. L. Chen, C. S. Wang and A. Manivannan, *Electrochim. Acta*, 2011, **56**, 3981–3987.
24 M. Q. Fan, B. Ren, L. Yu, Q. Liu, J. Wang, D. L. Song, J. Y. Liu, X. Y. Jing and L. H. Liu, *CrystEngComm*, 2014, **16**, 10389–10394.
25 X. D. Li, W. Li, M. C. Li, P. Cui, D. H. Chen, T. Gengenbach, L. H. Chu, H. Y. Liu and G. S. Song, *J. Mater. Chem. A*, 2015, **3**, 2762–2769.

